On-Chip Tightly Confined Guiding and Splitting of Surface Acoustic Waves Using Line Defects in Phononic Crystals

Feng Gao, Sarah Benchabane, Amine Bermak, Shurong Dong, Abdelkrim Khelif

On-chip tightly-confined guiding and splitting of surface acoustic wave in line defects of phononic crystals

Feng Gao[1,4*], Sarah Benchabane[2], Amine Bermak[3], Shurong Dong[4], Abdelkrim Khelif[2]

[1] ZJU-Hangzhou Global Scientific and Technological Innovation Center, Zhejiang University, Hangzhou, China
[2] Institut FEMTO-ST, CNRS, Université de Bourgogne Franche-Comté, F-25030 Besançon Cedex, France
[3] College of Science and Engineering, Hamad Bin Khalifa University, Education City, Doha, Qatar
[4] College of Information Science & Electronic Engineering, Zhejiang University, Hangzhou, China

* Corresponding author: Feng Gao (gao.feng@zju.edu.cn)

Abstract

Phononic crystals (PnCs) exhibit acoustic properties that is not usually found in natural materials, which leads to the possibility of new device designs for the complex manipulation of acoustic waves. In this article, we report the construction of a micron-scale phononic waveguide by line defects in phononic crystal for the on-chip tightly-confined guiding, bending and splitting of surface acoustic waves (SAWs). The PnC is made of square-lattice of periodic nickel pillars. It exhibits a complete bandgap that prohibits the propagation of SAW inside the PnC but allows the propagation within the line defects. The waveguides were implemented on a 128° Y-cut lithium niobate substrate by an electroplating-based microfabrication process. The PnC lattice constant, pillar diameter and pillar height are 10 μm, 7.5 μm and 3.2 μm, respectively. Interdigitated transducers are monolithically integrated on the same substrate for SAW excitation around 195 MHz. The guiding, bending and splitting of surface waves in the phononic waveguide are experimentally observed through measurement of the out-of-plane surface displacement fields using a scanning optical heterodyne interferometer. The high frequency tightly-confined phononic wave-guides demonstrate the feasibility of precise local manipulation of SAW that are essential for emerging frontier applications such as phonon-based quantum information processing.

KEYWORDS: *Phononic crystal, Surface acoustic wave, Acoustic waveguide, Acoustic bandgap*

1. Introduction

Surface acoustic wave (SAW) devices are widely used in applications including telecommunication[1, 2], sensing[3-5], and microfluidics[6, 7]. The operation of existing SAW devices is based on the manipulation of planar surface waves excited by interdigitated transducers (IDTs), which usually have acoustic aperture (beam width) more than ten times of the wavelength. In contrast, the localized manipulation of SAW at lateral scales close to the wavelength still remains challenging. Breakthrough in this field would be a significant extension of SAW technologies and is essential for the development of emerging frontier applications such as phonon-based quantum information processing[8, 9].

Phononic waveguide plays an important role in localized manipulation of SAW including guiding, turning and splitting. It is typically constructed by specific arrangements of phononic crystals (PnCs), which are made of periodic cells and can prohibit SAW propagation by acoustic bandgaps[10-12]. The bandgaps can be formed by different mechanisms including local cell resonance or Bragg reflection[13]. PnCs can be implemented on different substrate with various lattice structures such as triangle[14], square[10], and hexagon[15, 16]. Its unit cells can also be different forms such as cylinder hole[10], cylinder pillar[11], annular hole[17], etc.

Most of the research regarding phononic waveguides for surface waves focus on theoretical predictions. Back to 2006, Sun and Wu theoretically analyzed the possibility of guiding surface waves through sharp bends in line-defect phononic waveguides[18]. Later it was reported SAW waveguides can also be constructed by hollow-pillar cavity mode PnCs[19], self-collimation effect in PnCs[20] and edge waves in topological PnCs[21, 22].

Line-defect waveguides in phononic crystals made by periodic holes is one of the earliest reported experimental implementation of phononic waveguides[23]. Nevertheless, the early work was based on a silicon substrate and thus cannot be integrated with IDTs requiring piezoelectric substrates. A subsequent design demonstrated a phononic waveguide integrated with IDTs on a lithium niobate substrate[24]. However, only straight waveguiding was demonstrated, leaving arbitrary guiding to be explored. Fully functional waveguides for Lamb waves, a close analogy to surface waves, were however experimentally implemented in different forms including phononic waveguides[25, 26], suspended mechanical waveguides[27] and coupled-resonator elastic waveguides[28]. Recent advances in the field achieved the arbitrary guiding of surface waves. Fu *et al.* reported the guiding of surface waves through ridged rings and proved the feasibility of its potential application in phononic circuit[29]. While Fu's design is in a form of mechanical waveguide, Wang *et al.* demonstrated the first arbitrary phononic waveguide based on valley-locked surface waves in topological PnCs[30]. Nevertheless, the lateral confinement is relatively weak as the wave field penetrates a few wavelengths into the adjacent PnCs.

In this article, we report a tightly-confined phononic waveguide that supports arbitrary local manipulation of surface waves including guiding, turning and splitting. The phononic waveguide is constructed by line defects in a square-lattice PnC with unit cells made of nickel pillars. The guiding effect is achieved through optimization of pillar geometry, mode selection and channel design. IDTs were also monolithically integrated on the waveguide chip for the excitation of planar surface waves, which is then guided locally through the phononic waveguide. In contrast to topological phononic waveguides, the free surface in the channel of the line-defect phononic waveguide provides open interface for the integration of detection circuits or actuators. This feature combining the tightly-confined precise manipulation of surface waves enables the versatility of the line-defect phononic waveguide in emerging applications such as phonon-based quantum information processing and molecular sensing.

2. Results and Discussion

2.1 Configuration of the phononic waveguide

The phononic waveguide is constructed by line defects in square-lattice PnCs on a 128° Y-cut lithium niobate substrate as shown by Fig. 1a. IDTs with 10-μm pitch ($\lambda = 20\ \mu m$) are integrated on the same substrate for SAW excitation. The waveguides are experimentally implemented using an electroplating-based process. Fig. 1b shows an SEM image of a SAW splitter constructed by the phononic waveguide. It converts the planar surface wave from the IDTs to a guided wave and splits it into two branches. Other configurations including straight waveguide and 90°-bending waveguide are also implemented (Fig. S1 of Supporting Information). Fig. 1c shows the

schematic diagram of the lattice unit cell. The lattice constant (a) is 10 μm. Each unit cell contains a cylindrical nickel pillar of 7-μm diameter (d_p) and 3.2-μm height (h_p). The pillar dimensions are chosen by finite element method (FEM) optimization of the waveguide performance. The waveguide channel width (d_c) is defined as the edge to edge distance between the side pillars (Fig. 1a). Due to the limitations of the fabrication process, the actual nickel pillar shows a rounded top (Fig. 1d). Its diameter (7.7 μm) is also slightly larger than the designed value. The heights of the pillars range from 3.2 μm to 3.6 μm for different devices across the wafer due to the non-uniformity of electroplating.

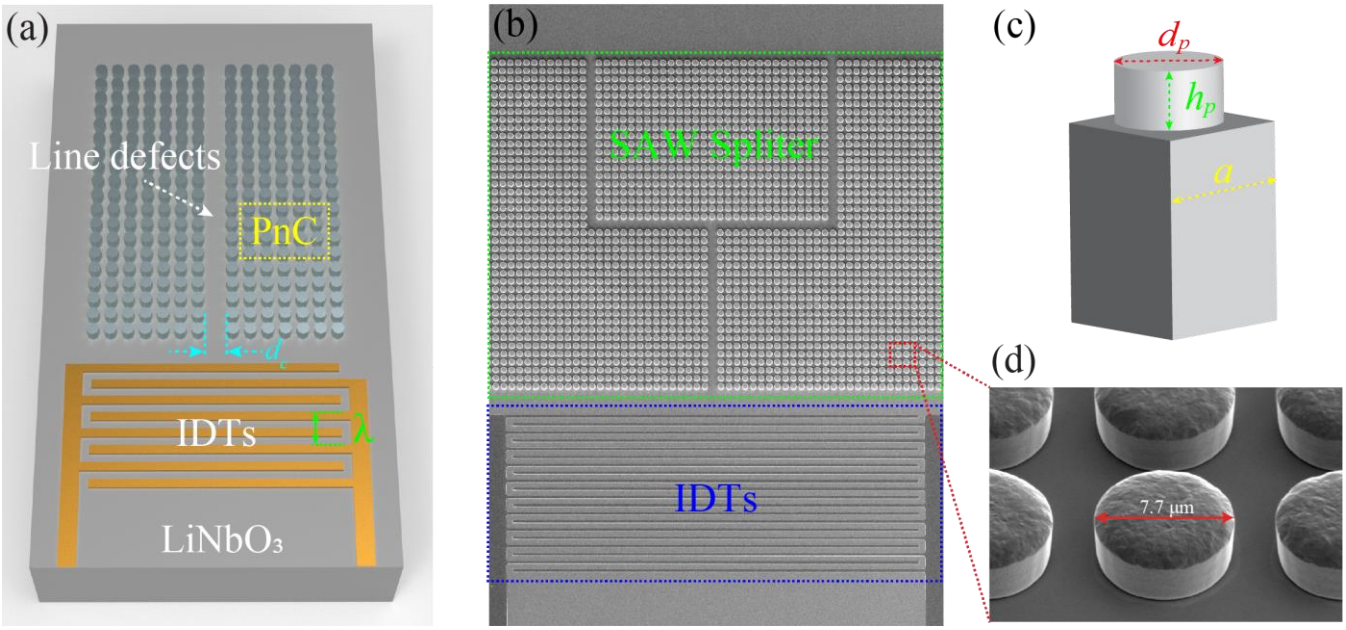

Figure 1. (a) Schematic diagram of a straight waveguide form by line defects in a square lattice PnC. (b) SEM image of the SAW splitter. (c) Unit cell of the PnC with lattice constant a, pillar diameter d_p, and pillar height h_p. (d) Close-in image of the nickel cylinders in the PnC.

2.2 Phononic bandgap for SAW prohibition

A complete bandgap of the PnC is required to achieve the prohibition of SAW propagation in all directions. Fig. 2a shows the FEM simulated band structure of the PnC along the closed wave vector (k) path $\Gamma - X - M - Y$ in the first irreducible Brillouin zone (Fig. 2a insert). The wave vector lies on the surface plane with $k =$ X aligning with the X axis of the lithium niobate substrate. The $\Gamma - X - M - Y$ path contains complete wave propagation characteristics because of the substrate lattice symmetry. As the FEM eigen frequency solver cannot distinguish bulk and surface modes, the data points of both modes are mixed in the band diagram. In order to highlight the band structure of surface waves, we modulated the transparency of the data point by the average displacement ratio between the surface and the bulk regions of the substrate. Opaque data points correspond to surface modes, while the data points with increasing transparency correspond to modes with higher bulk leakage. Pure bulk modes are removed in the band diagram as they are fully transparent. The detailed processing method is illustrated in Fig. S2 and Note I of Supporting Information. The blue region in Fig. 2a marks a complete Bragg bandgap where no surface waves can propagate in the PnC. Its lower boundary is determined by the surface mode frequency at the M point, which is 185.4 MHz. A vague upper boundary appeared around 213.2 MHz. The upper boundary is not explicit because it approaches the gradual transitioning regime of leaky modes and bulk modes. It should be noted that the other data points with frequencies fall in the bandgap are leaky surface modes or bulk modes, which does not affect the complete prohibition of surface waves.

The transmission characteristic of the PnC block made of 10-pillars is shown in Fig. 2b. The information of the simulation model is described in Fig. S3 and Note II of Supporting Information. Both the transmission along $k = X$ and $k = Y$ are simulated as shown by the blue and orange lines in Fig. 2b, respectively. The PnC band-gap is marked by the semi-transparent blue region. As expected, the transmission in the bandgap is low as surface modes are prohibited in the bandgap. The low transmission extends to the frequency regime above the bandgap due to the

high bulk leakage in this regime. Nevertheless, a small region below the bandgap also shows low transmission despite propagating modes exist in this region as shown by the violet data points in Fig. 2a. This is in fact because the violet data points correspond to breathing modes that cannot be excited by Rayleigh waves. Fig. 2c shows the mode shapes of the breathing mode and flexural modes at $k = \mathrm{Y}$, which correspond to P1 and P2 marked by the black stars in Fig. 2a, respectively. In contrast to the flexural mode that shares similar motion with Rayleigh waves, the circular motion of the breathing mode is incompatible with the elliptical particle movement of Rayleigh waves. The lower boundary of the stopband is thus determined by the highest excitable surface modes (flexural modes) marked by the yellow data points in Fig. 2a, which are 164.5 MHz and 153.8 MHz for $k = X$ and $k = Y$, respectively. These two frequencies agree with the stop-band transition frequency in Fig. 2b.

The effect of PnC on prohibiting SAW propagation is experimentally verified by a scanning laser interferometer (Fig. S4). Fig. 2d shows the measured out-of-plane surface displacement of a PnC in the propagation path of SAW excited by six pairs of IDTs (left side) at 200 MHz. The SAW amplitude represented by the measured surface displacement is significantly reduced after passing through the PnC. Fig. 2e shows the frequency spectrum of the SAW amplitudes before and after passing through the PnC block. The input (before PnC) and output (after PnC) amplitude sampling areas are marked by the red and green dashed rectangles in Fig. 2d, respectively. The input SAW reaches maximum amplitude at 195 MHz, which is determined by the IDT periodicity ($\lambda_0 = 20\mu m$) and the SAW velocity on the 128° Y-cut lithium niobate substrate ($v = 3900\ m/s$). After passing the PnC block, the output SAW amplitude drops to the noise floor of the optical measurement setup due to the strong bandgap prohibition effect of the PnC.

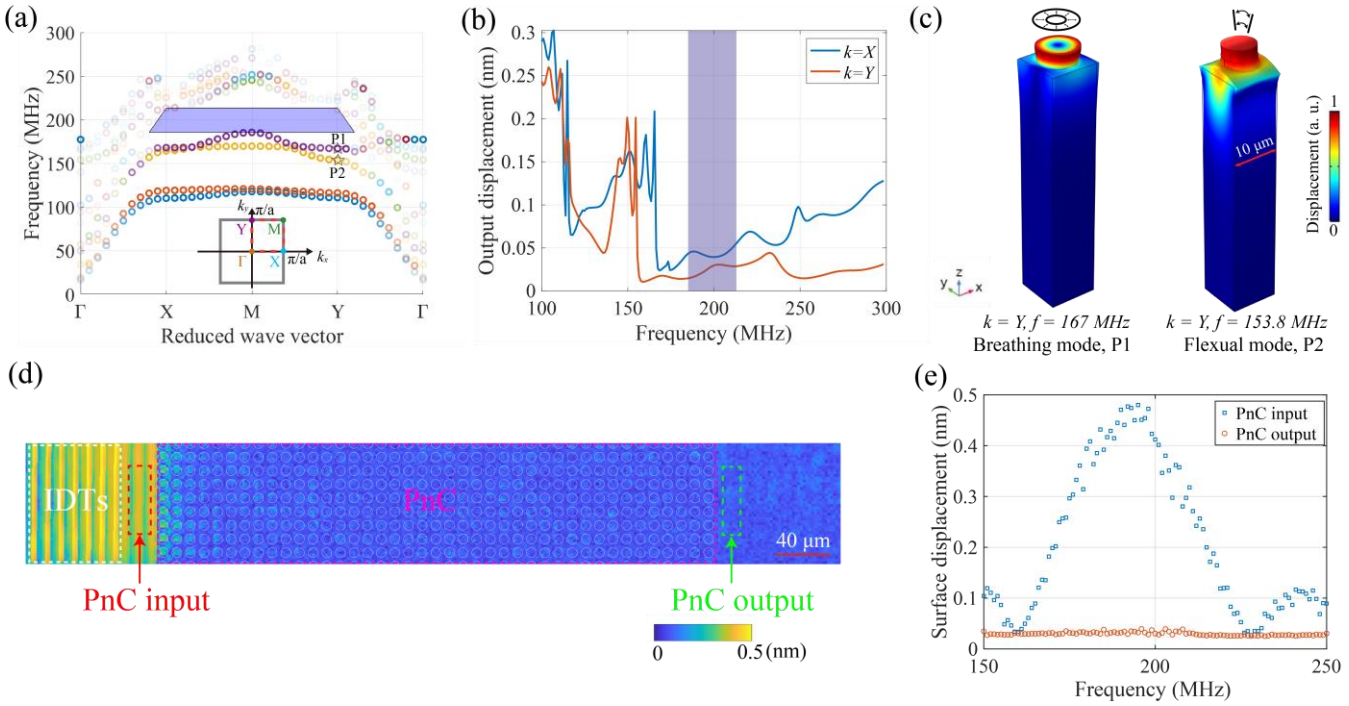

Figure 2. (a). Band structure of the PnC crystal with square lattice of nickel cylinder pillars. The blue region marks the complete SAW bandgap. Insert is the corresponding first irreducible Brillouin zone used in the band structure. (b) The transmission spectrum of a PnC block with 10-pillar depth. The bandgap regime marked by the blue region shows low transmission. (c). Mode shape of breathing and flexural modes at $k = Y$. (d) Measured surface displacement map showing SAW is blocked by a PnC with 41-pillar depth. (e) Surface displacement spectrum before and after the 41-pilar PnC.

2.3 Guided SAW characteristics in the line-defect channels

Unlike planar surface waves, the guided SAW in the line-defect channels must be compatible with the mode constraints of the adjacent nickel pillars of the PnC to sustain its propagation. Its properties can thus vary drastically from the planar SAW. Fig. 3a shows the mode shape of the guided SAW ($f = 201\ MHz,\ k = Y$) in a single-row line-defect waveguide unit cell ($h_p = 3\mu m$, $d_p = 7\ \mu m$, see Fig. S5 and Note III of S.I. for FEM model description).

Its displacement field is mostly confined in the center of the line-defect channel near the surface region. The X and Z cutline displacements (Fig. 3b) confirm that the wave amplitude decreases quickly away from the channel center and surface, respectively. It is known that surface waves with velocity higher than the shear bulk acoustic wave (S-BAW, slowest bulk wave) will be leaky waves. However, the observed non-leaky SAW (displacement field is confined around the surface) in the waveguide has a velocity ($v_{SAW} = f \times \lambda = 4020\ m/s$) higher than the S-BAW velocity ($v_{S-BAW} = 3700\ m/s$). It was reported that PnCs allow SAW modes propagate at velocities higher than the radiation limit[31]. The higher velocity in the phononic waveguide is a similar effect and could be possibly attributed to the existence of bound states in the continuum (BIC) modes[32]. The BIC modes allow propagation above radiation limit due to the localized confinement of wave energy by the periodic pillars.

Fig. 3c shows the simulated surface displacement map of a straight waveguide formed by a single-row line defect ($h_p = 3\ \mu m$, $d_p = 7\ \mu m$, see Fig. S6 and Note IV of Supporting Information for FEM model description). The waveguide channel aligns with the X axis of the $LiNbO_3$ substrate. A line source on the left side of the mode oscillates in Z direction to excite the surfaces waves. As shown by the displacement map, the planar SAW entering the PnCs on the upper and lower side of the model is quickly attenuated. As a result, the vibration amplitude of the pillars also decreases quickly along the SAW propagation direction. In contrast, the line-defect channel in the center allows the propagation of a guided surface mode. At the outlet of the channel, a circular diffraction pattern can be observed, which is because the output is a point source of surface waves. It can also be observed that the lateral penetration of the SAW displacement field into the PnC varies along the channel and exhibit a sinusoidal pattern. This is because of the formation of standing waves caused by the in-channel reflections.

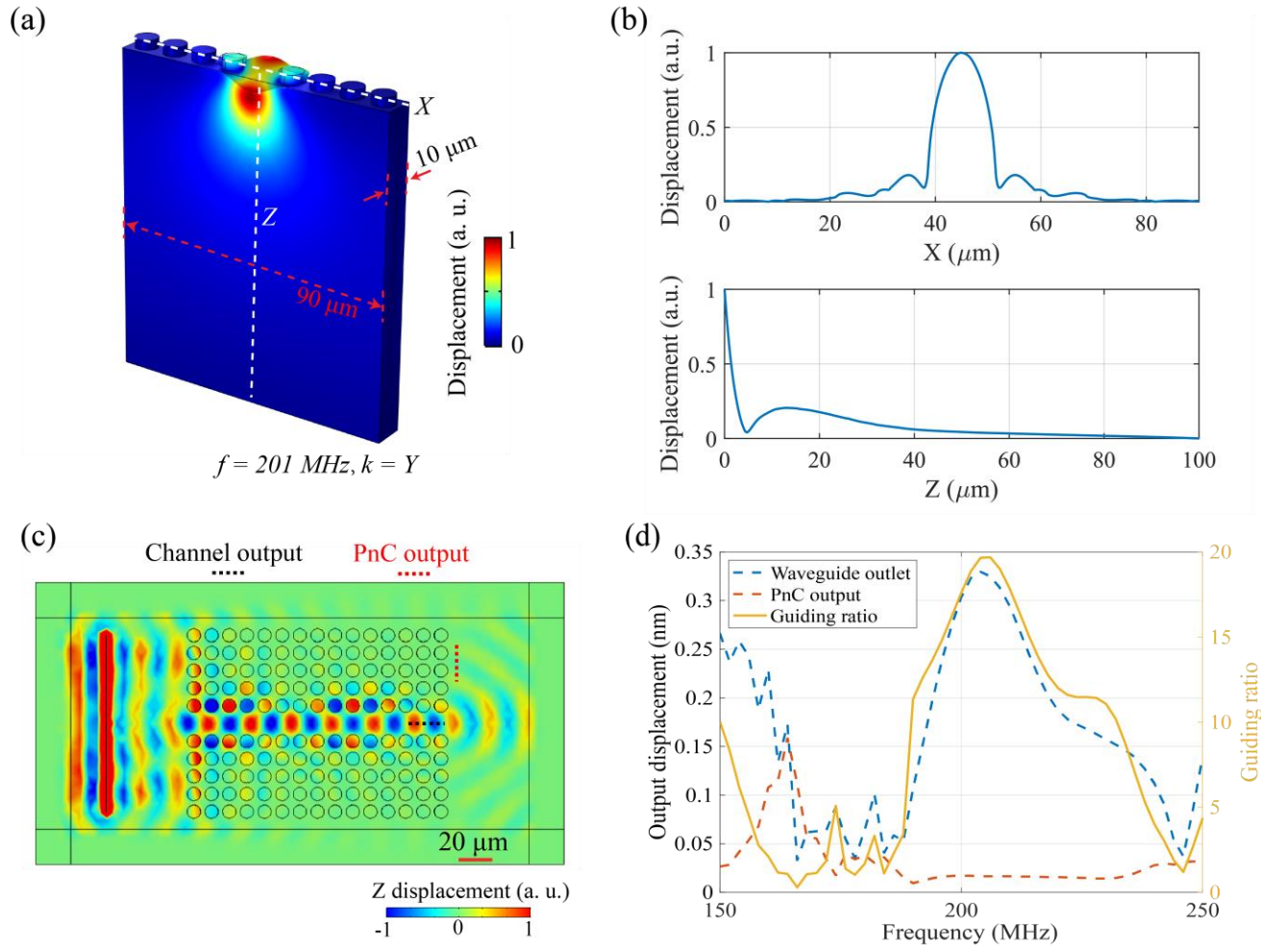

Figure 3. (a). Mode shape of a waveguide unit cell showing the tight confinement of displacement field. (b) The X and Z cutline displacements show the displacement decreases quickly away from the waveguide center and surface. (c) Displacement map of a straight waveguide ($h_p = 3\ \mu m$, $d_p = 7\ \mu m$) at 200 MHz excitation showing the guided SAW along the channel and a diffraction pattern at the outlet. (d). The frequency characteristics of the straight waveguide. Transmission peak is observed at 205 MHz.

The frequency characteristics of the straight waveguide is obtained by sweeping the oscillation frequency of the line source. The mean surface displacement amplitude at the end of the waveguide channel ($\bar{u}_{wg}$, black dashed line in Fig. 3c) and after the PnC ($\bar{u}_{PnC}$, red dashed line in Fig. 3c) are extracted to compare the transmission through the line defect channel and the PnC, respectively. The ratio between the two displacements is defined as the guiding ratio ($G = \bar{u}_{wg}/\bar{u}_{PnC}$) for evaluating the effectiveness of the waveguide. Large guiding ratio means that SAW is mostly transmitted through the line-defect channel with little leakage through the PnC. The frequency spectrum of $\bar{u}_{wg}$, $\bar{u}_{PnC}$ and G are shown by the blue dashed line, orange dashed line and yellow solid line in Fig. 3d, respectively. Low transmission through the PnC ($\bar{u}_{PnC}$) is observed from 174 MHz to 250 MHz due to the existence of the phononic bandgap. The transmission through the line-defect channel ($\bar{u}_{wg}$) reaches the maximum at 205 MHz with a 3- dB passband between 194 to 216 MHz. The guiding ratio spectrum around the passband follows the trend of the channel transmission spectrum as the PnC transmission remains flat in this regime.

2.4 Parametric optimization of the line-defect SAW waveguide

To optimize the performance of the phononic waveguide, parametric sweeping of its design parameters including pillar diameter, pillar height, and channel width is performed. Fig. 4a shows the guiding ratio (yellow line) of the straight waveguide when its pillar diameter varies from 1 to 10 μm. The pillar height is fixed at 3 μm for the sweeping. Results show that the guiding ratio reaches its maximum at 7-μm pillar diameter. Based on this optimum pillar diameter, a sweeping of pillar height from 1 to 10 μm is then performed. Fig. 4b shows that the guiding ratio have two peaks at 3.2 μm and 5.4 μm. The valley of the guiding ratio between the two peaks is mainly caused by the increase of wave leakage through the PnC (Orange-dashed line in Fig. 4b). Despite both guiding ratio peaks exhibit high guiding effectiveness, it was found only the pillar heights in the range of 2.6 to 3.8 μm supports SAW bending and splitting. This is because the pillars with height around 3.2 μm have elliptical flexural mode polarizations (Fig. 4c upper part) that is compatible with both the waves propagate in inlet channel and split channels. In contrast, the pillars with heights around 5.4 μm show linear flexural mode polarization (Fig. 4c lower part) that aligns with the wave propagation, which cannot be converted to the polarization in the perpendicular direction and thus does not support wave bending. The reduced vibration amplitude of the pillars at the end of the channels confirms this effect: the split channels tend to have a perpendicular pillar polarization and thus reduce the original pillar polarization of the inlet channel.

Fig. 4d shows the guiding ratio of the straight waveguide at different channel widths. The wave is completely blocked when the channel width is smaller than 10 μm (half wavelength), leading to low guiding ratio. It then increases with the increase of channel width and reaches a stable value. In contrast to the straight waveguide that can have arbitrary channel width, channel width of bending waveguide needs to be multiple of the lattice constant to have the pillars remain aligned in lattice around the turning corner. Fig. 4e and Fig. 4f show the simulated propagation of guided SAW through 90°-bending waveguides with 1-pillar and 2-pillar line defects, respectively. The results show that SAW can be guided through the 1-pillar line-defect bending, while the guided SAW turns into an asymmetric mode and attenuates quickly after passing the 2-pillar bending. Similar phenomenon is observed in SAW splitter with 1-pillar and 2-pillar line-defect waveguides (Fig. S7 of Supporting Information). It is thus necessary to use 1-pillar line defect to support bending and splitting in the phononic waveguide.

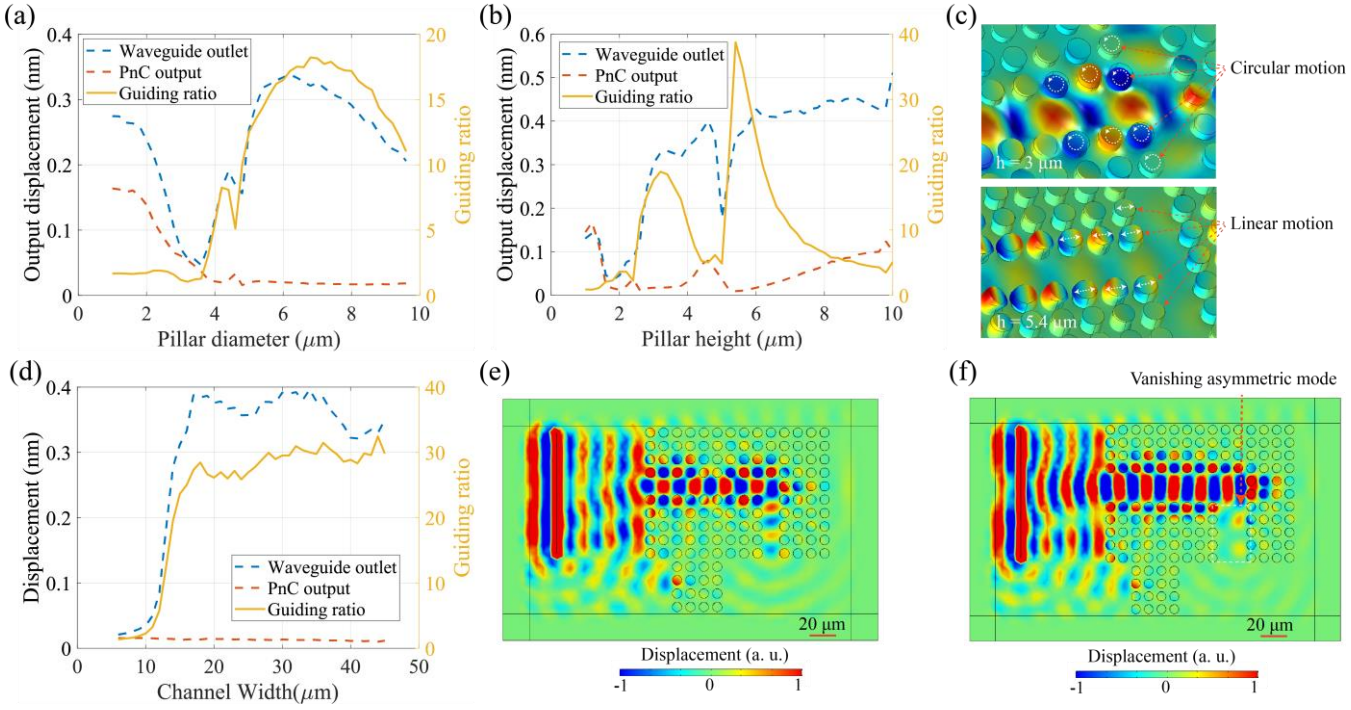

Figure 4. (a) Pillar diameter sweep shows a peak guiding ratio at $d_p = 7$ μm. (b) Pillar height sweep shows both $h_p = 3.2$ μm and $h_p = 5.4$ μm offers good guiding effectiveness. (c) Pillar height around 3 μm can support SAW bending due to the circular motion of the pillars (upper figure) while pillar height around 5.4 does not allow SAW bending due to the linear pillar motion. (d) The guiding ratio starts to increase when the channel width is greater than 10 μm and saturates when it is greater than 15 μm. (e). 1-pillar line defect channel can support SAW bending (f). 2-pillar line defect channel does not allow SAW bending because of the excitation of asymmetric mode after the bend.

2.5 Experimental characterization of the waveguide

Based on the optimized design parameters obtained by FEM, straight, 90°-bending and SAW splitter waveguides with 1-pillar line-defect channels were implemented using the electroplating-based process. Out-of-plane surface displacement of the three waveguides (Fig.5a-Fig.5c) were measured to visualize the guided SAW propagation. To highlight the line-defect channels, the PnCs in each of the waveguide are covered by light-gray overlay with white-dashed line boarders. IDTs on the left of the waveguides are used to excite the planar surface waves. The straight waveguide (Fig. 5a) demonstrates clear confinement and guiding of SAW along the line-defect channel. A diffraction pattern can be observed at the outlet of the waveguide, which agrees well with the simulation result in Fig. 3c. Measurement of the 90°-bending waveguide (Fig. 5b) shows the guided surface wave can be turned twice in the line-defect channel and still produce a diffraction pattern at the outlet. Nevertheless, a relatively large attenuation exhibit at the turning corners of the waveguide. The outlet diffraction pattern is also less regular than that of the straight waveguide, which is due to the disturbance of the leaked SAW from the PnC region. The surface displacement map of the SAW splitter in Fig. 5c demonstrate the dividing of SAW into two branches. The splitter is symmetric along the input channel. The zoomed images show the splitting point and upper outlet of the splitter, respectively. Similar to the 90°-bending waveguide, strong attenuation is observed at the splitting/bending corners. The diffraction pattern at the output is also distorted due to the interference by the SAW leaked directly from the PnC.

Fig. 5d shows the SAW amplitudes along the center of the straight waveguide from the inlet to the outlet. The amplitude curves exhibit standing wave ripples due to the internal reflection in the waveguide channel. Linear fitting of the two curves are used to extract the guided SAW attenuation rate. Fig. 5e shows the spectrum of the attenuation rate, which increases with the excitation frequency. The measured frequency range is from 190 MHz to 200 MHz due to the limitation of the IDT excitation bandwidth and the displacement measurement noise level of the interferometer. To obtain the wavelength and phase velocity, we also measured the SAW phase variation in the straight waveguide channel. The measured SAW waveform and phase data is given in Fig. S8 of Supporting Infor-

mation. Fig. 5f shows the wavelength and phase velocity of the guided SAW in the straight waveguide. The measured SAW wavelength (23.1 μm at 195 MHz) in the waveguide is higher than the Rayleigh SAW wavelength on the free surface (20.4 μm at 195 MHz). This means that the guided SAW has higher velocity than the Rayleigh SAW and suggests that the guided SAW is a BIC mode. The phase velocity decreased from 4568 m/s at 190 MHz to 4449 m/s at 200 MHz. The group velocity is 2986 m/s, which is derived from the wavelength and frequency information. The measured guided SAW wavelength and phase velocity show similar trend as the simulation result (Fig. S9), despite the later have slightly higher values ($\lambda = 24.1\ \mu m$ simulated vs $\lambda = 23.1\ \mu m$ measured at 195 MHz). The discrepancy could be attributed to the pillar profile and nickel material property difference between the simulation and experimental implementation.

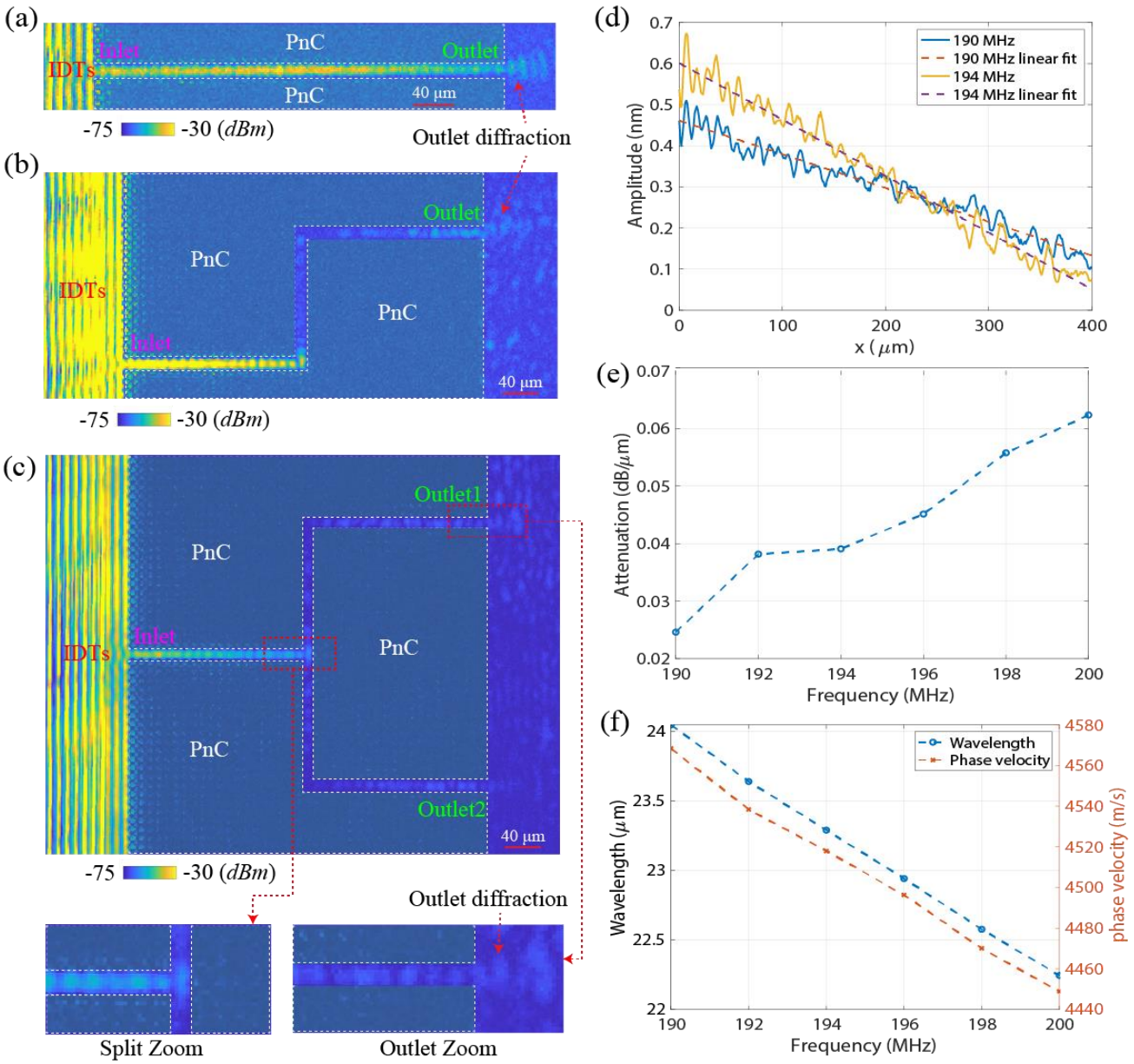

Figure 5. Out-of-plane surface displacement of (a). Straight waveguide (b) 90°-bending waveguide and (c) SAW Splitter (d). SAW amplitude along the center of the straight waveguide at 190 and 194 MHz. (e). SAW amplitude attenuation in the straight waveguide from 190 MHz to 200 MHz. (f). SAW wavelength and phase velocity in the straight waveguide channel from 190 MHz to 200 MHz.

The decreasing phase velocity in Fig. 5f implies the reduction of bulk leakage of SAW at higher frequency, which in turn should results in the reduction of propagation attenuation. However, the measured attenuation increases with the increase of excitation frequency, which means bulk leakage is not the limiting factor for attenuation. This agrees

with the simulation result in Fig. 3a, which shows a non-leaking guided mode with higher phase velocity than the S-BAW.

2.6 Discussion.

The phononic waveguides operate by the local confinement of SAW in PnC line defects utilizing the complete bandgap of the PnC. In fact, the complete bandgap (Fig. 2a) of the rectangular lattice is not a classic bandgap that is usually discovered between two propagating mode[10, 33]. It is between the highest propagating surface mode and the radiation limit determined by the S-BAW. Due to the presence of the periodic nickel pillars, this radiation limit is higher than the S-BAW velocity. The guided SAW in the phononic waveguide also exhibit a higher velocity than the S-BAW, which suggest that the guided mode should be leaky. Nevertheless, the simulation result in Fig. 3a shows that it is a perfectly confined non-leaky mode. This phenomenon is possibly due to that the guided mode is a symmetry protected BIC mode that is preserved by the periodicity of the PnC pillars[32].

The waveguide performance is described by its guiding ratio, which is determined by pillar height, pillar diameter and channel width. The increase of pillar diameter increases the reflection from each individual cell and thus improves the guiding ratio. However, the guiding ratio drops when the pillar diameter exceeds 7 μm. As the transmission through the PnC remains low when the pillar diameter is over 4 μm, the guiding ratio decrease is mainly caused by the decrease of the waveguide channel transmission, which could be due to the increase of attenuation or the distractive reflection along the channel at large pillar diameters. The guiding ratio vs pillar height curves shows two local optimums at 3.2 μm and 5.4 μm. However, the pillars with heights around 5.4 μm exhibit linear flexural mode polarization that does not support the turning of SAW. Conversely, the elliptical flexural mode polarization of the pillars around 3.2 μm high can seamlessly transit to the perpendicular channel and thus supports SAW turning. The channel width controls the SAW mode in the waveguide. When the line defect is a single column, symmetric mode propagates in the waveguide and can pass through the 90°-bend. In contrast, the guided SAW passing through the 2-pillar 90°-bend transforms to an asymmetric mode that attenuates quickly. It is thus necessary to construct the waveguide with 1-pillar line defects.

Although the on-chip SAW waveguide is successfully demonstrated, it still exhibits relatively high attenuation that should be addressed in the future. One of the possible solutions is to use a different lattice type such as triangular lattice or hexagonal lattice. Wave turning imposes the highest attenuation in the waveguide. The turning angle is limited to 90° in the rectangular lattice. Using other types of lattices supporting different turning angles can reduce this turning loss. Besides lattice type, the unit cell geometry can play an important role in the guiding performance as it affects the internal reflection and polarization. The SAW bending relies on the elliptical polarization of the cylinder pillars with proper heights. Other elements such as triangular pillars that tends to polarize in selected directions can possibly reduce the turning attenuation. On the other hand, using two different pillar geometries with one type assigned to the turning corners and another type assigned to the straight waveguide channels could enable the separate optimization of propagation loss and turning loss. Moreover, further optimization of the substrate crystal orientation can also help reduce the attenuation. Beside the 128° Y-cut, we also explored Y-cut lithium niobate but found it is unable to achieve the waveguiding effect. A further search of arbitrary crystal orientations could lead to the implementation of low-attenuation phononic waveguide.

3. Conclusion

In summary, we developed a micron-scale phononic waveguide for the on-chip guiding, bending and splitting of SAWs. The phononic waveguide is constructed by line defects in phononic crystals made of square-lattice of nickel pillars. The waveguide achieved tight lateral confinement due to the strong lateral Bragg reflection. Although the velocity of the guided mode is found to be higher than that of the Rayleigh wave on free surface, it is still a non-leaky mode with most of the displacement field confined near the surface, possibly due to the formation of BIC mode. Optimum design parameters including pillar diameter, pillar height and channel width of the waveguides are obtained through finite element analysis. The waveguides were experimentally implemented on a 128° Y-cut lithium niobate substrate with monolithically integrated IDTs. The guiding effects were experimentally characterized and visualized by measurement of its surface displacement field using a scanning optical heterodyne interferometer. This phononic waveguide demonstrates the feasibility of arbitrary on-chip manipulation of SAWs while achieving tight lateral confinement within a single wavelength. It can serve as an enabling technology for future applications

that requires precise local manipulation of acoustic energy or phonons such as quantum information processing and sensing.

4. Experimental Section

Simulation setup: The FEM modeling of the PnC and the waveguide was performed with Comsol Multiphysics. Solid mechanics, electrostatics and piezoelectric effect were solved on the geometry. The band diagram was obtained by eigen frequency simulation. The simulation model is given in Fig. S2 of Supporting Information. The depth of the substrate was set to five lattice constants (50 μm) with fixed boundary condition applied to the bottom. Floquet boundary conditions were applied to the front-back sides and left-right sides of the unit-cell. In the Floquet boundary condition, k_x and k_y were set to sweep the across the first irreducible Brillouin zone ($\Gamma - X - M - Y$), while k_z was set to zero. The bulk modes and leaky modes were then filtered out by lowering their data point transparency. The mode shape of the unit-cell waveguide is also obtained by Eigen frequency study with the model shown in Fig. S5 of Supporting Information.
The PnC transmission characteristics were simulated using a simplified one-column model shown in Fig. S3 of Supporting Information. Frequency domain simulation was used to resolve the displacement values from 100 MHz to 300 MHz. A line source with 1-nm prescribed displacement along Z axis was used to generate the SAW. The surface displacement after the 10 pillars is used to evaluate the transmission from the PnC. PMLs were added to the two ends of the model along the propagation axis to remove boundary reflection. Periodic boundary conditions were applied to the two sides parallel to the propagation axis, which effectively extends the column number to infinite. The depth of the model is 100 μm with fixed boundary condition applied to the bottom.

The simulation of the straight waveguide, 90°-bending waveguide and the SAW splitter were all performed in frequency domain study. The simulation model is shown in Fig. S6 of Supporting Information. A line source with 1-nm prescribed displacement was used for SAW generation. The surface displacement at the output of the waveguides were used to evaluate their transmission characteristics. PMLs were added to the surrounding of the models to remove reflection. The substrate depth is set to 60 μm with fixed boundary condition applied to the bottom.

Device fabrication: The waveguides were fabricated using an electroplating based process. The process flow chart is given in Fig. S10 of Supporting Information. After cleaning with piranha solution, 15-nm titanium and 100-nm copper were deposited on the 4-inch 128° Y-cut lithium niobate substrate. The copper layer was used as the seed layer for nickel electroplating while titanium layer was used to promote the adhesion of copper to the lithium niobate substrate. A complementary photoresist pattern (AZ9260, 6 μm thick) of the phononic crystal pillars were then added to the substrate by optical lithography. The photoresist pattern was used as the electroplating mold. Nickel electroplating is then performed at a current of 0.2A for 35 minutes. The thickness of the electroplated nickel ranges from 3-3.8 μm across the wafer due to the process variation. The photoresist is then removed by immersing the wafer in Microposit 1165 remover at 70°C for 30 minutes. Reactive ion etching (RIE) is then used to remove the copper and titanium layers on the blank region. Subsequently, IDTs were fabricated by a lift-off process. The complementary photoresist pattern (AZ nLof 2020, 3 μm) of the IDTs was firstly added to the wafer. E-beam evaporation is then used to deposit 10-nm titanium and 200-nm aluminum on the wafer. The wafer is then immersed in 70°C Microposit 1165 photoresit remover overnight to complete the lift-off process. The individual waveguide devices are then diced from the wafer using a mechanical dicing saw.

Measurement of surface displacement: A laser scanning heterodyne interferometer was used to measure the surface out-of-plane displacement of the waveguides. The interferometer is in a Mach-Zehnder configuration as shown in Fig. S4 of Supporting Information. The output of the 633-nm laser (Thorlabs HRS015B) is split into two frequency-shifted beams by an acousto-optic modulator (AA Opto Electronic MTS110-A3-VIS). The two beams are orthogonally polarized. The frequency-shifted beam is used as the reference beam and goes directly to the detector photodiode after passing through reflecting mirrors and a polarizing beam splitter (PBS). The other beam without frequency shift is used as the signal beam that goes to the device surface. It is focused on the device surface by a long-working distance microscope objective with a numerical aperture of 0.8 (Olympus LMPLFLN100x). The laser spot size on the device is about 650 nm. The reflected signal beam from the device surface recombines with the reference beam through the PBS. The phase of the signal beam is modulated by the out-of-plane surface displacement of the device. The interference of the two beams are detected by a fast photodiode (Alphalas UPD-200-SP).

The photodiode signal is amplified and detected by either a spectrum analyzer (Anritsu MS2830A) for obtaining the displacement amplitude or an oscilloscope (Agilent DSO9254A) for acquiring the displacement phase maps. The device is wire bonded to a printed circuit board (PCB) and connected to a signal synthesizer (Agilent N5181A) for SAW excitation. The scanning is implemented by mounting the PCB on a nano-positioning stage (Aerotech ANT95XY). The 2D displacement map is obtained by driving the stage to scan across the designated device area with 1.5 μm steps and measuring the displacement at each individual point.

Supporting Information

Supporting Information is available from the Wiley Online Library or from the author.

Acknowledgments

This work is funded by NPRP grant No. NPRP10-0201-170315 from the Qatar National Research Fund (a member of Qatar Foundation). This work is also supported by the EIPHI Graduate School (contract "ANR-17-EURE-0002") and the French RENATECH network with its FEMTO-ST technological facility. This project has received funding from the European Research Council (ERC) under the European Union's Horizon 2020 research and innovation program (grant agreement No. 865724). This project is also supported by National Key R&D Program of China (No. 2022YFB3604500), NSFC-Zhejiang Joint Fund for the Integration of Industrialization and information (No. U1909212 and No. U20A20172) and Zhejiang Province Key R & D programs (No. 2021C05004). The findings herein reflect this work and are solely the responsibility of the authors.

Conflict of interest

The authors declare no conflict of interests.

Author contributions

Feng Gao, Amine Bermak, Sarah Benchabane and Abdelkrim Khelif proposed the idea. Feng Gao and Sarah Benchabane designed the fabrication process and the characterization method. Feng Gao fabricated and tested the device. Feng Gao, Abdelkrim Khelif, Sarah Benchabane and Shurong Dong drafted the manuscript.

Data Available Statement

The data that support the findings in this study are available from the corresponding author upon request.

Reference

1. R. Su, J. Shen, Z. Lu, H. Xu, Q. Niu, Z. Xu *et al.*, Wideband and low-loss surface acoustic wave filter based on 15° YX-$LiNbO_3$ /SiO_2 /Si structure. *IEEE Electron Device Lett.* **2021**, 42, 438-441.
2. J. Shen, S. Fu, R. Su, H. Xu, Z. Lu, Z. Xu *et al.*, High-performance surface acoustic wave devices using LiNbO 3/SiO 2/SiC multilayered substrates. *IEEE Trans. Microw. Theory Tech.* **2021**, 69, 3693-3705.
3. M. Agostini, F. Lunardelli, M. Gagliardi, A. Miranda, L. Lamanna, A. G. Luminare *et al.*, Surface‐Acoustic‐Wave (SAW) Induced Mixing Enhances the Detection of Viruses: Application to Measles Sensing in Whole Human Saliva with a SAW Lab‐On‐a‐Chip. *Adv. Funct. Mater.* **2022**, 32, 2201958.
4. F. Gao, F. Boussaid, W. Xuan, C.-Y. Tsui, A. Bermak, Dual transduction surface acoustic wave gas sensor for VOC discrimination. *IEEE Electron Device Lett.* **2018**, 39, 1920-1923.
5. F. Gao, A. Bermak, S. Benchabane, L. Robert, A. Khelif, Acoustic radiation-free surface phononic crystal resonator for in-liquid low-noise gravimetric detection. *Microsyst. Nanoeng.* **2021**, 7, 8.
6. R. J. Shilton, V. Mattoli, M. Travagliati, M. Agostini, A. Desii, F. Beltram *et al.*, Rapid and Controllable Digital Microfluidic Heating by Surface Acoustic Waves. *Adv. Funct. Mater.* **2015**, 25, 5895-5901.
7. M. Wu, Z. Mao, K. Chen, H. Bachman, Y. Chen, J. Rufo *et al.*, Acoustic separation of nanoparticles in continuous flow. *Adv. Funct. Mater.* **2017**, 27, 1606039.
8. K. J. Satzinger, Y. Zhong, H.-S. Chang, G. A. Peairs, A. Bienfait, M.-H. Chou *et al.*, Quantum control of surface acoustic-wave phonons. *Nature* **2018**, 563, 661-665.
9. R. Manenti, M. Peterer, A. Nersisyan, E. Magnusson, A. Patterson, P. Leek, Surface acoustic wave resonators in the quantum regime. *Phys. Rev. B.* **2016**, 93, 041411.
10. V. Laude, M. Wilm, S. Benchabane, A. Khelif, Full band gap for surface acoustic waves in a piezoelectric phononic crystal. *Phys. Rev. E.* **2005**, 71, 036607.

11. A. Khelif, Y. Achaoui, S. Benchabane, V. Laude, B. Aoubiza, Locally resonant surface acoustic wave band gaps in a two-dimensional phononic crystal of pillars on a surface. *Phys. Rev. B.* **2010**, 81, 214303.
12. M. Oudich, N. J. Gerard, Y. Deng, Y. Jing, Tailoring Structure-Borne Sound through Bandgap Engineering in Phononic Crystals and Metamaterials: A Comprehensive Review. *Adv. Funct. Mater.* **2022**, 2206309.
13. D. Zhang, J. Zhao, B. Bonello, F. Zhang, W. Yuan, Y. Pan *et al.*, Investigation of surface acoustic wave propagation in composite pillar based phononic crystals within both local resonance and Bragg scattering mechanism regimes. *J. Phys. D: Appl. Phys.* **2017**, 50, 435602.
14. S.-Y. Yu, J.-Q. Wang, X.-C. Sun, F.-K. Liu, C. He, H.-H. Xu *et al.*, Slow surface acoustic waves via lattice optimization of a phononic crystal on a chip. *Phys. Rev. Appl.* **2020**, 14, 064008.
15. S.-Y. Yu, X.-C. Sun, X. Ni, Q. Wang, X.-J. Yan, C. He *et al.*, Surface phononic graphene. *Nat. Mater.* **2016**, 15, 1243-1247.
16. S. Mohammadi, A. Khelif, R. Westafer, E. Massey, W. D. Hunt, A. Adibi, Full band-gap silicon phononic crystals for surface acoustic waves, *ASME International Mechanical Engineering Congress and Exposition*, **2006**.
17. B. Ash, A. Rezk, L. Yeo, G. Nash, Subwavelength confinement of propagating surface acoustic waves. *Appl. Phys. Lett.* **2021**, 118, 013502.
18. J.-H. Sun, T.-T. Wu, Propagation of surface acoustic waves through sharply bent two-dimensional phononic crystal waveguides using a finite-difference time-domain method. *Phys. Rev. B.* **2006**, 74, 174305.
19. Muhammad, C. Lim, J. Reddy, E. Carrera, X. Xu, Z. Zhou, Surface elastic waves whispering gallery modes based subwavelength tunable waveguide and cavity modes of the phononic crystals. *Mechanics of Adv. Mater. and Struc.* **2020**, 27, 1053-1064.
20. Z.-D. Zhang, F.-K. Liu, S.-Y. Yu, M.-H. Lu, Y.-F. Chen, An integrable and configurable phononic beam splitter based on self-collimated surface acoustic waves. *Appl. Phys. Express.* **2020**, 13, 044002.
21. P. Wang, L. Lu, K. Bertoldi, Topological phononic crystals with one-way elastic edge waves. *Physical review letters* **2015**, 115, 104302.
22. Y. Liu, X. Chen, Y. Xu, Topological Phononics: From Fundamental Models to Real Materials. *Adv. Funct. Mater.* **2020**, 30, 1904784.
23. P. H. Otsuka, K. Nanri, O. Matsuda, M. Tomoda, D. Profunser, I. Veres *et al.*, Broadband evolution of phononic-crystal-waveguide eigenstates in real-and k-spaces. *Sci. Rep.* **2013**, 3, 1-5.
24. S. Benchabane, O. Gaiffe, R. Salut, G. Ulliac, V. Laude, K. Kokkonen, Guidance of surface waves in a micron-scale phononic crystal line-defect waveguide. *Appl. Phys. Lett.* **2015**, 106, 081903.
25. D. Hatanaka, H. Yamaguchi, Real-space characterization of cavity-coupled waveguide systems in hypersonic phononic crystals. *Phys. Rev. Appl.* **2020**, 13, 024005.
26. Y. Guo, M. I. N. Rosa, M. Gupta, B. E. Dolan, B. Fields, L. Valdevit *et al.*, Minimal Surface‐Based Materials for Topological Elastic Wave Guiding. *Adv. Funct. Mater.* **2022**, 2204122.
27. Y. D. Dahmani, C. J. Sarabalis, W. Jiang, F. M. Mayor, A. H. Safavi-Naeini, Piezoelectric transduction of a wavelength-scale mechanical waveguide. *Phys. Rev. Appl.* **2020**, 13, 024069.
28. Y.-F. Wang, T.-T. Wang, J.-P. Liu, Y.-S. Wang, V. Laude, Guiding and splitting Lamb waves in coupled-resonator elastic waveguides. *Compo. Struc.* **2018**, 206, 588-593.
29. W. Fu, Z. Shen, Y. Xu, C.-L. Zou, R. Cheng, X. Han *et al.*, Phononic integrated circuitry and spin–orbit interaction of phonons. *Nat. Commun.* **2019**, 10, 1-7.
30. J.-Q. Wang, Z.-D. Zhang, S.-Y. Yu, H. Ge, K.-F. Liu, T. Wu *et al.*, Extended topological valley-locked surface acoustic waves. *Nat. Commun.* **2022**, 13, 1-8.
31. C. Pouya, G. R. Nash, Sub-and supersonic elastic waves in an annular hole phononic metamaterial. *Commun. Mater.* **2021**, 2, 1-8.
32. C. W. Hsu, B. Zhen, A. D. Stone, J. D. Joannopoulos, M. Soljačić, Bound states in the continuum. *Nature Reviews Materials* **2016**, 1, 1-13.
33. G.-G. Xu, X.-W. Sun, R.-S. Li, Z.-R. Zhang, T. Song, Z.-J. Liu, The low-frequency bandgap characteristics of a new three-dimensional multihole phononic crystal. *Appl. Phys. A* **2021**, 127, 1-10.